Contents lists available at ScienceDirect

Nano Energy

journal homepage: www.elsevier.com/locate/nanoen

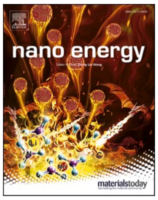

2D Ruddlesden-Popper perovskite ferroelectric film for high-performance, self-powered and ultra-stable UV photodetector boosted by ferro-pyro-phototronic effect and surface passivation

Linjuan Guo [a,1], Yaqian Qi [a,1], Zheng Yang [a,1], Lei Zhao [a], Wei Zhang [a], Xinzhan Wang [a], Haixu Liu [a], Guoying Yan [a,*], Shufang Wang [a,*], Caofeng Pan [b,*]

[a] *Hebei Key Laboratory of Optic-Electronic Information and Materials, National & Local Joint Engineering Laboratory of New Energy Photoelectric Devices, College of Physics Science and Technology, Hebei University, Baoding 071002, PR China*

[b] *CAS Center for Excellence in Nanoscience, Beijing Institute of Nanoenergy and Nanosystems, Chinese Academy of Sciences, Beijing 100083, PR China*

ARTICLE INFO

Keywords:
2D Ruddlesden-Popper perovskites
Ferroelectric film
Self-powered UV photodetector
Ferro-pyro-phototronic effect
Surface passivation

ABSTRACT

2D Ruddlesden-Popper (RP) perovskites have attracted enormous attention in optoelectronic fields compared with their 3D counterparts. However, most of the reported perovskite ferroelectrics-based self-powered photodetectors (PDs) are fabricated from bulk single crystals rather than perovskite thin films with improved reproducibility, flexibility, and less preparation time. Nevertheless, the defect sites at surfaces and grain boundaries of 2D perovskites polycrystalline films make them vulnerable to humidity. Herein, the highly crystallized 2D RP perovskite ferroelectric films are successfully obtained. Then, a passivation method is applied on 2D perovskite film by an in-situ reaction with 4-fluoro-phenylethylamine iodide (4-FPEAI), which reduces the defect sites and endows the perovskite films with the outstanding hydrophobic property. Then, the as-prepared 2D-perovskite ferroelectric thin films were fabricated into self-powered PDs. Boosted by the ferro-pyro-phototronic effect, the self-powered PDs demonstrate excellent optoelectronic performances at 360 nm, with dark current less than 1×10^{-12} A, a peak responsivity over 1 A W^{-1}, a detectivity of 1.5×10^{14} Jones and fast response/recovery speed. The photoresponsivity and specific detectivity are both enhanced by 67.8 times regarding the relative peak-to-peak current, compared with those only based on the photovoltaic induced photocurrent. Further, the PDs show high stability towards high humidity and thermal treatment.

1. Introduction

3D metal halide hybrid perovskites have attracted enormous attention in the field of optoelectronic devices, owing to their excellent photoelectric properties, including high absorption coefficient, tunable bandgap, and long charge diffusion length [1–4]. However, the hybrid perovskites are hindered by the inherent drawbacks of instability towards moisture and oxygen. 2D RP perovskites with a chemical formula of $A'_2A_{n-1}M_nX_{3n+1}$, where A′ is a long aliphatic or aromatic alkylammonium cation, A is MA^+ ($CH_3NH_3^+$), Cs^+ or FA^+ ($NH_2CH_3NH_3^+$), M is Pb^{2+} or Sn^{2+}, X is Cl^-, Br^-, or I^-, and n is the number of $[MX_6]^{4-}$ octahedral monolayers between the organic spacer A′ layers, have emerged as a promising system for fabricating high-performance optoelectronic devices with long-term stability [5–7]. Compared with 3D perovskites, 2D RP perovskites exhibit significantly improved humidity stability owing to their hydrophobic terminating ligands. Besides, their structure diversity and tunability endow the rational designing of ferroelectrics [8], such as $(PMA)_2PbCl_4$ [9] (PMA = benzylammonium), $(BA)_2(MA)_2Pb_3Cl_{10}$ [10] (BA = $C_4H_9NH_3^+$), and $(BA)_2CsPb_2Br_7$ [11]. In such perovskite ferroelectrics, the combination of multi-functional ferroelectricity and outstanding optoelectronic properties will generate photoferroelectrics featuring switchable spontaneous polarization (P_s), which can create a built-in electric field to separate the photo-generated carriers without applying external bias, very favorable to fabricating self-powered PDs [12]. When the photoferroelectrics-based p-n junctions or schottky junctions are suddenly exposed to light illumination, the light-induced temperature rise will result in a disturbance of ferroelectric potential along the

---

* Corresponding authors.
E-mail addresses: mygy@hbu.edu.cn (G. Yan), sfwang@hbu.edu.cn (S. Wang), cfpan@binn.cas.cn (C. Pan).

[1] Linjuan Guo, Yaqian Qi and Zheng Yang contributed equally to this work.

https://doi.org/10.1016/j.nanoen.2022.107714
Received 14 June 2022; Received in revised form 10 August 2022; Accepted 15 August 2022

polarization direction, instantly generating a photovoltaic-pyroelectric coupled current. When light is turned off, an opposite pyroelectric current induced by a fall of temperature will be generated. What's more, the changes of ferroelectric polarization charges near the interface can effectively modulate the photoelectric process of photo-generated carriers. Therefore, the ferro-pyro-phototronic effect can significantly boost the performance of the PDs [13,14]. However, most of the reported perovskite ferroelectrics-based self-powered PDs are fabricated from bulk single crystals [15,16] rather than perovskite thin films with improved reproducibility, flexibility, and less preparation time. Therefore, the preparation of high-quality 2D RP perovskite ferroelectric films with high crystallinity, vertical orientation, excellent optoelectronic properties, and high operational stability is in urgent need.

The performance of 2D RP perovskite films-based devices is mainly restricted by two factors: 1, the crystallographic orientation; 2, the phase distribution or well width (n value). The former determines the charge transport efficiency since the insulating organic ligands hinder charge transport and thus impair devices' performance [17,18]. The latter decides the optical and electrical properties of 2D RP perovskite [19]. In addition to changing the composition of the 2D RP perovskite component, the goal of developing multi-functional ferroelectrics can be achieved by regulating the n value. Up to now, many efforts have been made to control the crystallographic orientation or distribution of quantum wells width for fabricating high-performance optoelectronic devices [20]. Zhang et al. demonstrated a uniform thickness distribution of quantum wells *via* hot-casting method, which could greatly enhance carrier transport along the perpendicular direction [21]. Huang's group reported phase-pure quantum well films with microscale vertically aligned grains by introducing molten salt spacer n-butylamine acetate (BAAc) as the precursor. Since Ac^- can coordinate with the perovskite framework [22]. The strong interactions between Pb^{2+} and carboxylate groups effectively promote the vertical growth of grains, which is also applied in the preparation of high-stable α-$FAPbI_3$ perovskite films [23], and compact tin perovskite films with a preferential crystal orientation and enhanced stability [24]. Therefore, it is a great way to introduce the carboxylate-based ionic liquid to control the perovskite crystallization toward high-quality films.

Besides, the long-term operational stability, especially wet stability, has become the most severe challenge for halide perovskites optoelectronic devices. Although 2D perovskites polycrystalline films exhibit improved humidity stability compared with their 3D counterparts, the defect sites located at surfaces and grain boundaries make the decomposition of the 2D perovskite easier, resulting from the invasion of moisture and oxygen [25]. For example, Min et al. demonstrated a 2D perovskite-based PD with large responsivity and ultrafast response speed [26]. However, the PD maintained only 60% of its initial response after being stored in 70% relative humidity (RH) conditions at room temperature (RT) for just seven hours. Therefore, a passivation method that can reduce the defect sites through chemical treatment of the undercoordinated surface lead centers and endue the perovskite films with an outstanding hydrophobic property at the same time is needed to improve the stability of 2D perovskite-based PDs [27].

Herein, we successfully prepared the highly crystallized 2D RP perovskite films ($(BA)_2(MA)_{n-1}Pb_nBr_{3n+1}$, $<n> = 2–5$ in this study) with microscale, defect-free, and vertically aligned grains by introducing ionic liquid BAAc into the precursor solution, optimizing the solvent composition and spin-coating temperature. The optimized phase distribution, crystalline orientation, and high crystallinity endow the 2D perovskite films with favorable optoelectronic properties and desired ferroelectricity. In addition, an in-situ passivation method further reduced the defect sites and improved hydrophobic property of the 2D perovskite film. Finally, the 2D perovskites/PC61BM heterojunction-based self-powered PDs demonstrate excellent optoelectronic performances. Especially, the self-powered PDs with $<n> = 4$ showed a lower dark current of 1×10^{-12} A, a higher peak *R* of 1 A W^{-1}, a lower *D** of 1.5×10^{14} Jones and fast response speed of 240 μs under 360 nm illumination. Compared with photocurrent induced only by photovoltaic effect, the *R* and *D** are both enhanced by 67.8 times regarding the relative peak-to-peak current. More than that, PDs exhibited high reproducibility and stability under the high humidity (80 ± 5%) and high temperature (80 °C) conditions for 32 days.

2. Experimental

2.1. Materials

The SnO_2 colloid solution oxide (15 wt% in H_2O colloidal dispersion), N, N-Dimethylformamide (DMF, 99.9%), Dimethyl sulfoxide (DMSO, 99.9%), 4-Fluorophenethylamine (4-FPEA, 98%), Hydroiodic acid (57 wt%), Anisole (99.9%), Polyethylneimine (PEIE, 80% ethoxylated solution), Chlorobenzene (99.5%), Cyclohexane (99.5%) and Tert-amyl alcohol (99.5%) were purchased from Shanghai Macklin Biochemical Co., Ltd. Lead bromine ($PbBr_2$, 99.99%), Methylammonium bromine (MABr, 99.99%), Butylamine acetate (BAAc, 99.99%), [6,6]-Phenyl C61 butyric acid methyl ester (PC61BM), Poly[(9, 9-dioctylfluorenyl-2, 7-diyl)-alt-(4, 4′-(N-(4-butylphenyl) (TFB), and Poly(3, 4-ethylenedioxythiophene)-poly(styrenesulfonate) (PEDOT:PSS 1000) were purchased from Xian Polymer light Technology Corp. All the chemicals were used as received without further purification. 4-FPEAI was prepared by the reaction of 4-FPEA with HI. Indium tin oxide (ITO)/glass substrate (sheet resistance ≤ 6 Ω) were purchased from South China Science & Technology Co., Ltd.

2.2. Preparation of precursor solution

The $BA_2MA_{n-1}Pb_nBr_{3n+1}$ ($<n> = 2, 3, 4, 5$) perovskite precursor solution was prepared by fully dissolving BAAc, MABr and $PbBr_2$ in DMF and DMSO (volume ratio: 1:1, 2:1, 3:1, 4:1). For the $<n> = 2–5$ systems, the detailed concentrations are listed in Table 1.

2.3. Fabrication of the PDs

The devices with a structure of ITO/ $BA_2MA_{n-1}Pb_nBr_{3n+1}$/PC61BM/Bi/Ag were fabricated in ambient air (temperature~23 °C, RH~40%). Firstly, ITO substrates were ultrasonically washed in acetone, ethanol, and deionized water for 15 min successively. After blowing with dry N_2 flow, the substrates were treated with O_2 plasma (80 W) for 10 min. Then the substrates were treated with PEIE solution following the literature [28] to enhance the wettability of the precursor solution and decrease hydroxyl groups which create charge traps and voids [29]. Briefly, the ITO substrates were fully immersed in 0.4 wt% PEIE aqueous solution for 30 s and then rinsed in deionized water for 3 s, followed by rapid thermal annealing at 100 °C for 10 min. Perovskite precursor solution was then spin-coated at 4000 r.p.m. for 20 s with 4000 ramp with substrate temperature fixed at a constant temperature (60–120 °C). After spin coating, the substrates were quickly removed from the spin coater and annealed at 100 °C for 10 min. After annealing, the perovskite films were cleaned and healed according to the literature with some modifications [30]. Cleaning solutions were prepared by mixing cyclohexane and tert-amyl alcohol in a volume ratio of 4:1. Healing solutions were prepared by adding 0.2 mg mL^{-1} MAI and 0.2 mg mL^{-1} 4-FPEAI to the above solutions. Then, PC61BM in chlorobenzene solution (10 mg mL^{-1}) was deposited onto the perovskite films. Finally, 20

Table 1
The concentration of the precursor solutions.

<n >	BAAc	MABr	$PbBr_2$
2	0.32 M	0.48 M	0.32 M
3	0.213 M	0.426 M	0.32 M
4	0.16 M	0.4 M	0.32 M
5	0.128 M	0.384 M	0.32 M

nm Bi and 80 nm Ag were deposited by a thermal evaporator (0.5 Å s^{-1}) using a shadow mask. Here, Bi layer acts as a permeation barrier that both insulates the perovskite from intrusion by moisture and protects the metal electrode from halide corrosion.

2.4. *Characterization*

The XRD patterns were obtained by the Bruker D8 Advance X-ray diffractometer equipped with a Cu tube ($\lambda = 1.5406$ Å). UV-vis absorbance spectrum was measured using a Hitachi U4100 UV-Vis-NIR spectrophotometer at RT, with a wavelength range of 250-800 nm. UPS measurements were recorded using a photoelectron spectrometer (Thermo, ESCALAB 250 Xi) to analyze the working function of the perovskite films. Steady-state and time-resolved PL measurements were taken using an FLS920 (Edinburgh Instruments) fluorescence spectrometer with 325 nm excitation wavelength. The morphological analyses of the films and devices were examined by conducting scanning electron microscopy (Nova NanoSEM450). GIWAXS measurements were performed using small angle wide angle X-ray scatterometer (Xeuss 2.0, Xenocs). Samples prepared on Si/SnO_2 substrates used an X-ray beam ($\lambda = 1.542$ Å) at an incident angle of 0.20° for 30 s, and the scattered light was collected by detector system at a distance of 150 mm vertically from the sample. For femtosecond TA spectroscopy, pulses at 360 nm (2 μJ cm^{-2} $pulse^{-1}$) generated through optical parametric amplification were used as the pump source. The spectra were recorded by an inverted confocal laser microscope (CLM, Nikon Ti-E) equipped with a spectrometer (Acton SpectraPro SP-2300), a Si charge-coupled device (CCD) camera (Nikon DIGITAL SIGHT DS-Ri1). The PFM measurement was carried out on a commercial PFM (Bruker Multimode 8), with an AC voltage applied to the conductive probe (Conductive Pt/Ir-coated silicon probes, EFM, Nanoworld). Trap-state densities were determined using the SCLC method. The structure is ITO/PEDOT:PSS/perovskite/TFB/Ag for hole-only devices. PEDOT/PSS solution was spin-coated at 5000 r.p.m. for 60 s in air and then annealed at 150 °C for 30 min. After the spin coating of the perovskite layer, the TFB layer (8 mg mL^{-1} in chlorobenzene) was spin-coated at 2000 r.p.m. for 60 s. Finally, the 80 nm Ag electrode was deposited using a thermal evaporation through a shadow mask. The structure is ITO/SnO_2/perovskite/PC61BM/Ag for electron-only devices. The dilute SnO_2 solution (2.5 wt%) was spin-coated on the ITO at 3000 r.p.m. for 30 s and annealed at 150 °C for 30 min. After the spin coating of the perovskite layer, the PC61BM layer (10 mg mL^{-1} in chlorobenzene) was spin-coated at 2000 r.p.m. for 60 s. Finally, 80 nm Ag electrode was deposited using thermal evaporation through a shadow mask. The dark *I-V* curves were obtained using the Keithley 4200 source meter.

2.5. *Photodetection performance measurements and stability tests*

The *I-V* characteristics and the *I-t* curves of the PDs were recorded by coupling a Stanford SRS current preamplifier (SR570) and a Stanford SRS function generator (DS345). The temporal responses of the device were performed on a digital oscilloscope (Tektronix, MDO3104). The laser was periodically switched by transistor-transistor logic (TTL) potential to generate pulsed laser beams. The 360, 405, 450, 532, 1064 and 1550 nm lasers (Changchun New Industries Optoelectronics Technology Co., Ltd.) were used as the light sources and shined from the back of devices. The light power intensity was calibrated using a silicon photodiode (PM100D). All devices were stored in the ambient atmosphere without any encapsulation during the measurements. The humidity stability and thermal stability of the unencapsulated PDs were performed by storing devices in 80 ± 5% RH at RT and continuously heated at 80 °C in an N_2-filled glove box. All PDs were tested under 360 nm laser illumination (127.3 μW cm^{-2}) for *I-t* characterization at regular intervals. The RH in the laboratory was within 30 ± 10% during the entire test.

3. Results and discussion

2D RP perovskites $(BA)_2(MA)_{n-1}Pb_nBr_{3n+1}$ were chosen as the model materials to prepare RP perovskite ferroelectric films since $(BA)_2(MA)_2Pb_3Br_{10}$ [31], and $(BA)_2(MA)Pb_2Br_7$ [16] singe crystals had been proven to possess prominent ferroelectric properties. $(BA)_2(MA)_{n-1}Pb_nBr_{3n+1}$ films, with different designed well widths ($<n> =2, 3, 4, 5$), were prepared *via* one-step hot spin-coating method. BAAc was used to provide butylamine ions to replace BABr. The absent bromine ions were offered by adding additional MABr into the solution. Fig. 1a illustrates the schematic procedures for the preparation of 2D perovskite film. First, the solvent composition of the precursor solution and the optimum spin-coating temperature during the hot-casting process were systemically explored. The 2D perovskite precursor solutions ($<n> = 3$) were firstly prepared by dissolving stoichiometric BAAc, MABr, and $PbBr_2$ in DMF/DMSO binary solvent with different volume ratio (0:1, 1:1, 2:1, 3:1, 4:1, 6:1 and 1:0). The preliminary spin-coating temperature was set at 90 °C. The morphologies of the 2D perovskite films were studied by scanning electron microscopy (SEM), and the crystallinity and crystal orientation of the 2D perovskite films were investigated by X-ray diffraction (XRD) patterns. From Fig. S1, one can see that all the seven films show dense and smooth surfaces with microscale grains whose average size decreases with the increase of DMF content. In the meantime, from the XRD patterns of insets in Fig. S1, two dominant diffraction peaks at 14.1° and 28.4°, corresponding to the (111) and (202) crystal planes of 2D perovskite, respectively, were observed, indicating good crystal orientation. With the increase of the DMF content, the intensities of the two peaks gradually increase, suggesting the enhanced crystallinity of perovskite films. Meanwhile, the peaks which belong to (0k0) crystal planes gradually disappear, indicating that the crystal orientation of the perovskites is enhanced, eliminating grains with orientation not perpendicular to the substrates. However, further increasing the DMF content will lead to the decrease of the peak intensity since DMSO can retard the crystallization rate [32], resulting in a better crystallinity. Therefore, the optimized volume ratio of DMF and DMSO is fixed at 4:1. Then, the influence of spin-coating temperature was investigated, set at 60, 70, 80, 90, 100, 110, and 110 °C, respectively. From the SEM images in Fig. S2, one can see that as the spin-coating temperature rises, the grain size gradually increases. However, when the temperature reaches 110 °C, many cracks occur at the grain boundaries, which may lead to current leakage. Besides, higher temperatures will lead to more volatilization of the organic components in 2D perovskite films. The highest XRD intensity was obtained for the film prepared at 100 °C. Therefore, the final spin-coating temperature was 100 °C. Then, $(BA)_2(MA)_{n-1}Pb_nBr_{3n+1}$ films ($<n> =2, 3, 4, 5$) were prepared using the above-mentioned optimized conditions. Further, the optical and electrical properties of the films were systematically studied. The $(BA)_2(MA)_{n-1}Pb_nBr_{3n+1}$ films with $<n> =2, 3, 4,$ and 5 are defined as P2, P3, P4, and P5, respectively. Fig. 1b illustrates the morphology of 2D perovskite films ($<n> =4$) from the top-view and cross-section view SEM images, respectively, with an average grain size of 3.1 μm and a thickness of 295 nm. The P4 film was composed of identical monolithic grains throughout the films, essential for efficient charge transporting in PDs. The SEM images of the P2, P3 and P5 films are shown in Fig. S3, all showing smooth and pinhole-free surfaces with the grain sizes of 1.8, 2.2 and 4.1 μm, respectively. The corresponding thicknesses are 290, 278, and 265 nm, respectively.

Fig. 1c shows the XRD patterns of the P2, P3, P4, and P5 films. For films with $<n> =3, 4, 5$, only two diffraction peaks at 14.1° (111) and 28.4° (202) were observed. Diffraction peaks that belong to (0k0) crystal planes don't exist in the above three XRD patterns, indicating that the three obtained films barely contain small-n phase compositions which are not perpendicular to the substrates. However, for the P2 film, in addition to the above two peaks, clear two-dimensional crystallographic planes (0k0) were observed, meaning the appearance of a more randomly distributed crystal orientation, which is consistent with

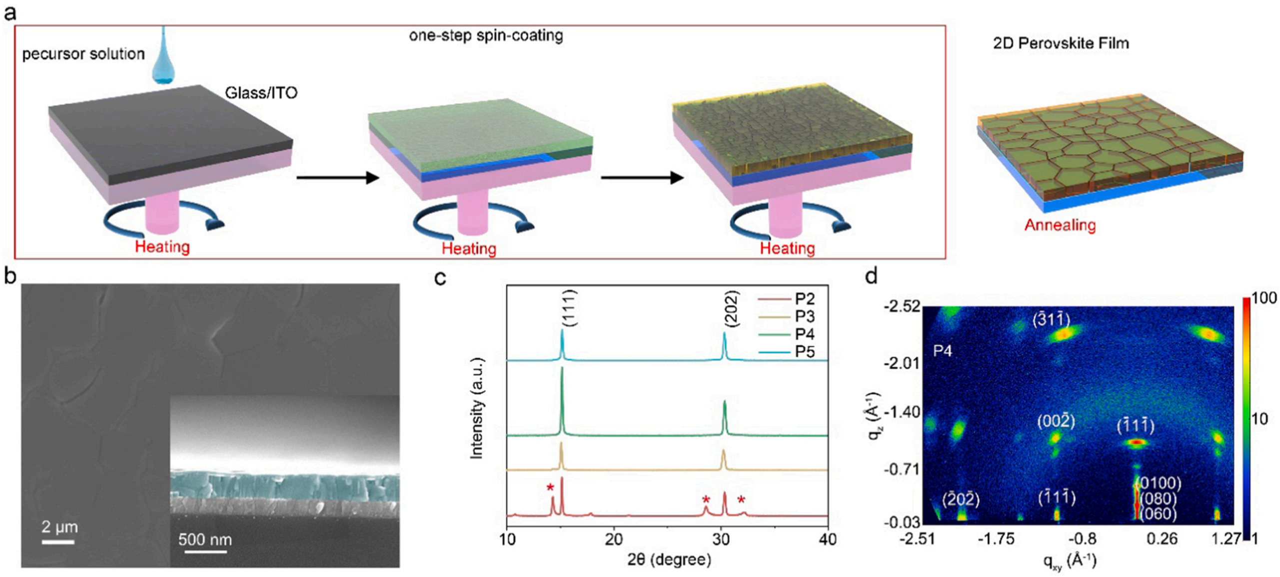

Fig. 1. (a) Schematic diagram of the film preparation procedures. (b) The top view and cross-sectional view (inset) SEM images of the P4 film. (c) XRD patterns of P2-P5 films. (d) GIWAXS image of the P4 film with Miller indices; color scale is proportional to X-ray probing signal intensity. q_z and q_{xy} represent in-plane and out-of-plane directions, respectively.

previous reports [22,33]. To further reveal the orientation of the RP perovskite, grazing-incidence wide-angle X-ray scattering (GIWAXS) analysis was conducted. The scattering patterns of the P4, P2, P3, and P5 films are shown in Figs. 1d and S4, respectively. The preferential crystal growth of the (111) and (202) planes with discrete Bragg spots were observed. The apparent and sharp Bragg spots were also observed in our films, such as (060), (080), and (0100) diffractions, demonstrating more crystal orientation perpendicular to the substrate. The high quality of the RP perovskite films was further confirmed by photographs measurement (Fig. S5).

To characterize the phase distribution in the four films, in-depth optical characterizations were conducted. The normalized absorption spectra of the P2, P3, P4, and P5 films taken through top-excitation and bottom-excitation are shown in Fig. 2a and d, respectively. Both top-taken and bottom-taken absorption spectra show multiple exciton absorption peaks at ≈ 430, 450, 475, and 515 nm, which can be assigned to $(BA)_2MA_{n-1}Pb_nBr_{3n+1}$ of $n = 2$, 3, 4, and ∞ phase compositions, respectively, indicating that the films have random well width distribution. Furthermore, the transient absorption (TA) tests were conducted to reconfirm the phase distribution in 2D perovskite films samples from both the top and bottom. The relative contributions of different n phases were quantified by their amplitude of the photobleaching (PB) peaks. Upon bottom excitation, P4 film exhibited initially strong PB peaks owing to lower-n phases (Figs. 2b and S6a), while the intensities of PB peaks for lower-n phases remarkably decreased when undergoing top excitation (Figs. 2e and S6b). The TA results verify that lower-n phases

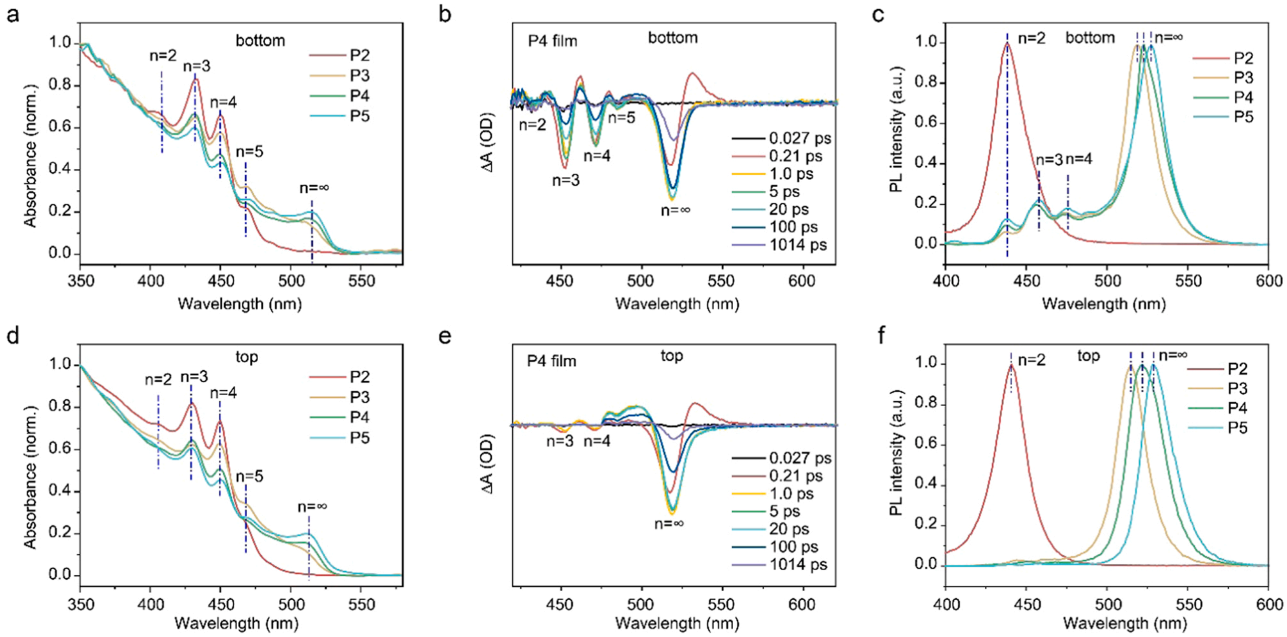

Fig. 2. The absorbance spectra of P2-P5 films taken from (a) the top side and (d) the bottom side. Chirp-corrected photo-induced changes in absorption (ΔA) spectra of P4 film taken from (b) the top side and (e) the bottom side. Steady-state PL spectra of P2-P5 films illuminated from (c) the top side and (f) the bottom side.

($n = 2, 3, 4$) and $n = \infty$ phase are vertically distributed from the bottom to the top surface. This phase alignment along the perpendicular direction is consistent with previously reported 2D perovskite films [26,34]. Then, the top-excited and bottom-excited photoluminescence (PL) spectra were conducted to further check the distribution of the phase compositions in the vertical direction of these films under the excitation of 360 nm light with the same optical power. When excited from the top surface of the perovskite films, only the emission peaks at the wavelength corresponding to $n = \infty$ phase were observed, undergoing a redshift from 510 to 525 nm with n rising. This redshift is induced by the weakening of the quantum confinement effect dominated by the small-n phase compositions [35], which is beneficial to the transport of charge carriers. When excited from the bottom, besides the emission peaks corresponding to $n = \infty$ phase, other emission peaks located at 430, 460, and 480 nm corresponding to the $n = 2$, 3, and 4 phase compositions also appeared, once again proving that lower dimensional phases tend to locate at the interface between perovskite films and ITO electrodes. The peak positions of film of $n = 2$ and $n = 3$ matched well with the values obtained from the reported single crystals. The mixed-phase distribution and vertical orientation guarantee the ferroelectricity throughout the film, facilitating the separation and extraction of charge carriers in 2D RP perovskites, which is beneficial to fabricating the ferro-pyro-photoelectric effect based self-powered PDs.

In addition to the better crystallinity and phase distribution, the passivation effect is vital to the performance of the PDs. Therefore, a trace amount of 4-FPEAI was introduced to the films by a simple solution method whose detailed procedures can be seen in Experimental Section. From the SEM image and XRD patterns in Fig. S7, one can see that there was no detectable change in the surface morphology as well as crystallinity, indicating the 4-FPEAI treatment did not destroy the perovskite films. The defects at surface and grain boundaries can effectively be reduced by 4-FPEAI treatment, as confirmed by both PL spectra and time-resolved PL (TRPL) measurements. Fig. 3a shows the top-excited PL spectrum of the P4 film before and after 4-FPEAI treatment. The PL intensity for the 4-FPEAI treated film is higher than that of untreated one. The PL lifetimes of the P4 films before and after 4-FPEAI treatment were evaluated using TRPL measurement (Fig. 3b). Both the decay curves show a biexponential feature, with the shorter one representing the surface recombination and longer one representing the bulk recombination, respectively. The 4-FPEAI treated P4 film showed a longer lifetime than that of the untreated film, once again indicating suppressed surface trap density. Furthermore, the 4-FPEAI treatment allows the perovskite films with an excellent hydrophobicity, which could protect the films from the invasion of humidity and oxygen. We compared the water-resistance of the untreated and 4-FPEAI treated P4 films by recording time-dependent contact angle, as shown in Fig. S8. The contact angle for water on the surface of the untreated P4 film has significantly decayed from 58° to 22.3° within 1 min, indicating the severe corrosion by water. While the 4-FPEAI treated P4 film can hold a large contact angle (> 95°) during the same period, confirming the excellent hydrophobicity, forming a strong contrast with the untreated one. The PL lifetimes of the four $(BA)_2(MA)_{n-1}Pb_nBr_{3n+1}$ films were also

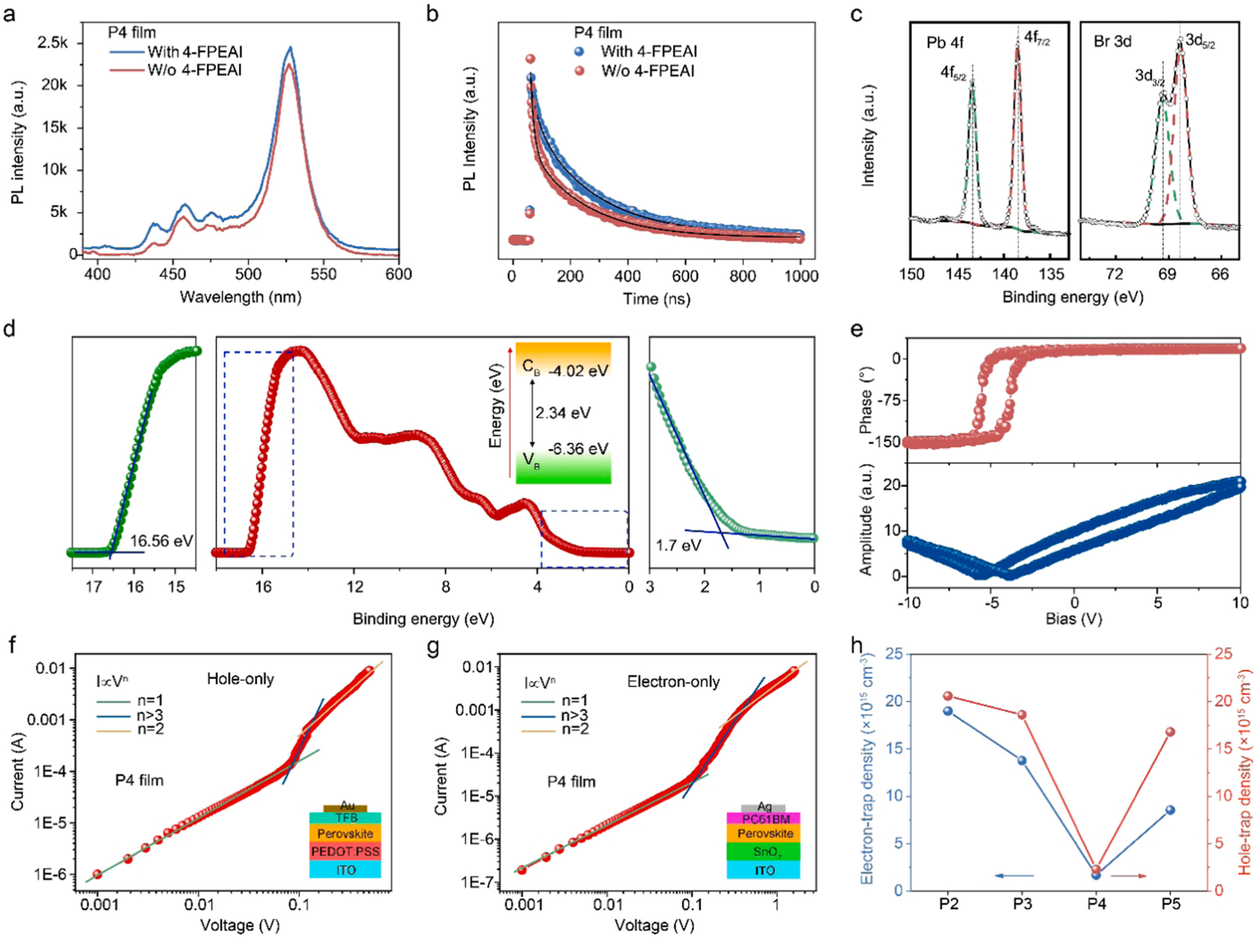

Fig. 3. (a, b) Steady-state and time-resolved PL spectra of P4 film with and without 4-FPEAI modification under an excitation wavelength of 360 nm. (c) XPS spectra of Pb 4f and Br 3d for P4 film. (d) UPS spectrum of the P4 film. The inset is the corresponding energy band diagram. (e) Dependence of phase and amplitude signals with applied DC bias of the P4 film, showing a hysteresis loop and a butterfly curve. *I-V* curves of the (f) electron-only device and (g) hole-only device based on P4 film. h) trap density (calculated from SCLC) of the P2-P5 film.

evaluated using TRPL (Fig. S9a). The lifetimes of P4 film are larger than those of P2, P3, and P5 films (Fig. S9b), proving the suppressed carrier recombination in the P4 film. In addition, the chemical states of Pb and Br in the perovskite films were determined using X-ray photoelectron spectroscopy (XPS) spectrum (Fig. 3c). The peaks of Pb 4f (138.40 and 143.25 eV) and Br 3d (68 and 65 eV) can be attributed to the Pb-Br bonds. Peak rising from Pb^0 (uncoordinated Pb^{2+}) was not observed, confirming there exists no bromine vacancies. Besides, the peaks of I 4d (630.7 and 619.2 eV) were also found (Fig. S10), proving the successful modification of 4-FPEAI.

From ultraviolet photoelectron spectroscopy (UPS) results in Fig. 3d, the valence band edge position and the Fermi level of the top of P4 film were estimated, with the Fermi level and the valence band edge locating at − 4.66 eV and − 6.36 eV, respectively, relative to the vacuum level. Therefore, the conduction band located at − 4.02 eV will be deduced according to the bandgap (Fig. S11). To verify the ferroelectricity of our 2D perovskite films, piezoresponse force microscopy (PFM) was utilized to characterize the P4 film. Fig. S12 demonstrates the vertical amplitude image and PFM phase image in the P4 film. As shown in the amplitude image of Fig. S12b, one can see that only a few regions have strong signals while the others have weak signals, behaving dark features in the amplitude contrast. Besides, the phase signals are very evident, showing a clear contrast with faint yellow and dark brown colors, indicating the presence of domain walls (Fig. S12c, red circles). Moreover, the polarization switching behavior is further verified by conducting PFM in spectroscopy mode and the results are shown in Fig. 3e. Clear hysteresis and butterfly loops are observed with a window bias of ± 10 V, demonstrating the room temperature ferroelectric polarization switching in the P4 film. Here, the hysteresis loop is characterized by a shift towards a positive voltage up to 20 V. The direction of the electric field is vertical to the surface of the P4 film, parallel to the direction of the spontaneous polarization. Then, the ferroelectricity of the four films was certified by the polarization-electric field (*P-E*) hysteresis loops. The loops in Fig. S13 all behave as evident ferroelectric hysteresis that possesses residual polarization (P_r) and coercive field (E_c). Among the four films, the P4 film possesses the highest P_r. The corrected electric field (E_c) of P4 film is − 16.6 kV cm^{-1}, with the corresponding voltage of the 0.42 V. From the absorption and PL spectra in Fig. 2, it is known that all four films contain ferroelectric phases (n = 2 and 3). The highly oriented perovskite grains result in ferroelectric phases perpendicular to the substrate. Therefore, the four films behave with ferroelectric properties, providing a foundation for ferro-pyro-phototronic effect boosting PDs. The trap densities of the four perovskite films were determined by space charge limited current (SCLC) method. Both hole-only devices (ITO/PEDOT:PSS (4083)/perovskite/TFB/Ag) and electron-only devices (ITO/SnO_2/perovskite/PC61BM/Ag) were fabricated, and the dark current-voltage (*I-V*) curves of P4 devices were recorded (Fig. 3f and g). The dark *I-V* curves for the other three PDs are shown in Fig. S14. Trap densities can be calculated by the following equation:

$$n_{trap} = \frac{2\varepsilon_0 \varepsilon_r V_{TFL}}{eL^2} \tag{1}$$

where ε_0 is the vacuum permittivity, ε_r is the relative dielectric constant, V_{TFL} is the trap-filled limit voltage, *e* is the electron charge, and *L* is the film thickness. Here, ε_r was determined from the capacitance-frequency measurement by impedance analyzer (Fig. S15), V_{TFL} is deduced from the dark *I-V* curves. Therefore, the hole-trap densities and electron-trap densities for the four films were calculated and plotted in Fig. 3h. The trap densities of the perovskite films are comparable with the single crystals, which may derive from reduced carrier recombination induced by good crystallinity, surface passivation, and intrinsic ferroelectricity.

Later, we introduced organic semiconductor PC61BM to fabricate self-powered PDs, with a device structure of glass/ITO/perovskite/PC61BM/Bi/Ag. Here, the Bi layer is introduced to protect the Ag electrode from bromine corrosion [36]. During the spin-coating procedure, 4-FPEAI with benzene ring will promote the self-assembly of PC61BM layer [37] and be beneficial for charge transport *via* π-π stacking [38]. As shown in Fig. S16a, upon 4-FPEAI treatment, the PL intensity of perovskite/PC61BM is greatly quenched compared with that without 4-FPEAI. This PL quenching indicates the higher charge carrier extraction efficiency across the interface. As a result, the PL lifetimes are also substantially shortened (Fig. S16b). The schematic structure of the self-powered PD is illustrated in Fig. 4a. From the cross-sectional SEM image of a typical P4 film-based device in Fig. 4b, one can see a well-formed interface between PC61BM and perovskite film, which will result in outstanding rectification behavior of the perovskite/PC61BM heterojunction. The relevant energy band diagram of the PD at zero bias is shown in Fig. 4c, relative to the vacuum energy level. The energy level obtained from UPS spectra of P4 with different etching depths is shown in Fig. S17. Due to the different phase distribution at the top and bottom of the perovskite film, the gradient energy level will be formed, which can promote the separation and transport of carriers. The highest occupied molecular orbital (HOMO) and lowest unoccupied molecular orbital (LUMO) of PC61BM are − 6 and − 4 eV, respectively. Since the 2D perovskite films possess ferroelectricity, the ferro-pyro-phototronic effect is anticipated to boost our PDs. Then, the systematic research and summary on photoresponses of the four self-powered PDs towards laser illumination were measured. Before testing, 0.5 V bias was applied to the devices for at least 1 min to obtain positive ferroelectric polarization. Figs. 4d and S17 show the *I-V* curves of the P4, P2, P3, and P5 film-based PDs under 360 nm laser illumination with different power intensities. The rectification characteristic in dark conditions indicates the formation of heterojunction. Besides, evident photoresponses induced by photovoltaic effect were found. It is worth noting that the P4 film-based PD not only exhibited a low dark current of less than 10^{-12} A, but also a large open-circuit voltage (0.5 V), guaranteeing the self-powered photodetecting ability. The dark currents of the four PDs without external bias were shown in Fig. S19. Fig. 4e shows the photoresponse of the P4 film-based PD under 360 nm laser periodical illumination (0.245 μW cm^{-2}) without external bias, behaving a typical four-stage photoresponse behavior. To understand the variation of output current under light and dark conditions, one typical cycle of the current curve is extracted from Fig. 4e and plotted in Fig. 4f. The mechanism is shown in Fig. 4g. Firstly, the sharp current peak at stage I is induced by pyroelectric current and photovoltaic current when light is turned on. The corresponding maximum output current is labeled as $I_{pyro+photo}$. The pyroelectric currents are generated since the light-induced temperature rise will disturb the random oscillation state of electric dipoles in the ferroelectric perovskite films. Thus, the total spontaneous polarization charges are reduced, resulting in current flow. Then, the temperature stays stable as the laser illumination continues. As a result, the pyroelectric current disappears, and only photovoltaic current stays at a steady plateau labeled as I_{photo}. When turning off the laser, a reverse pyroelectric current ($I_{pyro'}$) induced by the temperature decrease of the perovskite films was observed, owing to the raised spontaneous polarization charges. Finally, the temperature remains at RT without illumination. Thus, the pyroelectric current vanishes, and the output current returns to dark current. The energy band diagrams of the heterojunction under dark and 360 nm illumination conditions are shown in Fig. 4h and i. Upon UV illumination, photo-generated electrons and holes are produced at the interface between 2D perovskite and PC61BM, separated by the built-in electric field induced by the heterojunction and ferroelectricity, and finally collected by the ITO and Bi/Ag electrodes, respectively, forming the corresponding photocurrent. Besides, the reduced negative polarization charges at the heterojunction interface will lead to an downward bending of the energy band diagram of PC61BM and perovskite layers (orange line in Fig. 4i). Moreover, the ferroelectric potential and downward bending of the energy band are beneficial to the transport of charge carriers, resulting in a larger output current. To further confirm the existence of pyroelectricity, the *I-t* curves of the PD under dark conditions by raising the temperature (using a

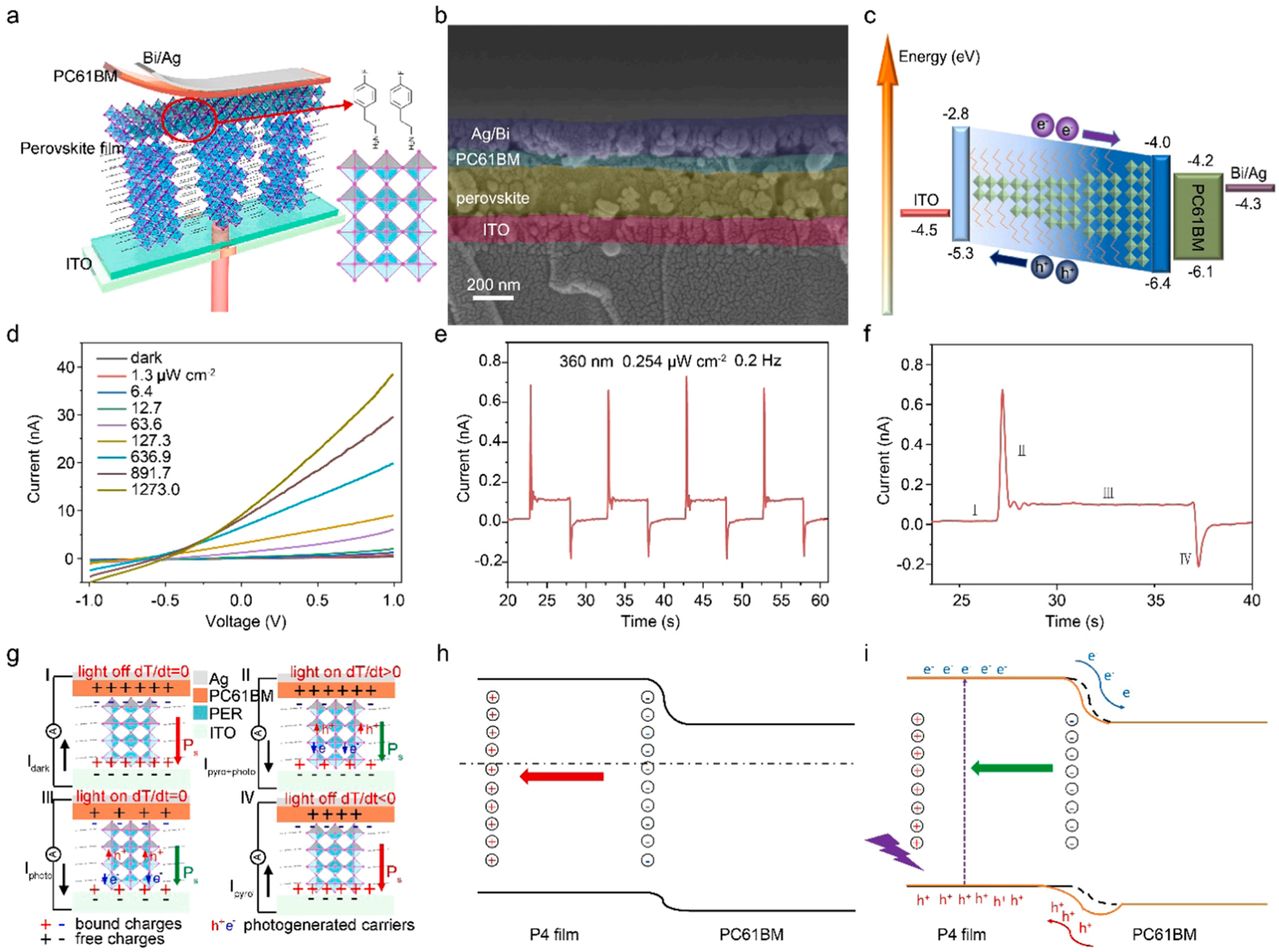

Fig. 4. (a) Schematic diagram of the structure of the PD. (b) Cross-sectional SEM image of a typical PD fabricated in this study. (c) Energy band diagram of the PDs, using the electron energy in the vacuum as a reference. (d) *I-V* characteristics under 360 nm illumination with different power densities ranging from 0 to 1.27 mW cm^{-2} of the P4 film-based PD. (e) Photoresponse behavior of the P4 film-based PD under 360 nm laser illumination with the power density of 0.254 μW cm^{-2} under zero bias. (f) An enlarged view taken from (d), displaying a typical four-stage photoresponse behavior. (g) Schematic working mechanism of the ferro-pyro-phototronic effect of the PD as turning on and turning off the laser. Energy band diagrams of the PDs under (h) dark and (i) light conditions.

10.6 μm CO_2 laser as the heating source) are measured (Fig. S20), from which one can see that positive current peaks appeared when the temperature increased. When laser was turned off, the temperature drop would lead to a negative pyroelectric current.

As demonstrated in Fig. S21, the output current signals of P4 film-based PD towards UV, visible, and near-infrared lasers illumination exhibit obvious four-stage photo-response dynamic behavior. The PD showed the highest output current towards a 360 nm laser, behaving with excellent UV photoresponses. Therefore, 360 nm laser was selected as the primary light source. Based on the systematic analysis of the working mechanism, we next compared the figures of merit of the four PDs (P2-P5). Fig. 5a presents the dark *I-V* curves of the four PDs. Among the four devices, the P4 film-based PD exhibits the lowest dark current, reflected by the better diffraction signals and lower measured trap density. From the *I-V* curves under 360 nm laser illumination, the P4 film-based PD manifests the highest photocurrents and largest open-circuit voltage (Fig. 5b). The *I-t* curves of all devices were measured under the same intensity of 360 nm laser at 0 V bias and plotted in Fig. 5c. All the four PDs demonstrate obvious four-stage photoresponse behavior, consistent with their ferroelectric properties. Compared with other devices, the P4 film-based PD exhibit an improved photocurrent and pyroelectric current. Three currents, $I_{pyro+photo}$, I_{photo}, and the relative peak-to-peak output current $I_{pyro+photo}$-I_{pyro}' are used to evaluate the photosensing performances of the pyro-phototronic effect based PDs [39–41]. Therefore, we used the highest output current $I_{pyro+photo}$-I_{pyro}' to compare the performances of P2-P5 PDs. The $I_{pyro+photo}$-I_{pyro}' of the four PDs are presented in Fig. 5d, from which one can see that the P4 film-based PD shows the highest output current while the P2 has the lowest one. The response time of P4 devices was determined as 260 μs for rise and 420 μs for decay under 360 nm laser illumination (Fig. 5e), which is much faster than those of P2, P3 and P5 films-based PDs (Fig. S22). The average maximum responsivities and detectivities of each PD are plotted in Fig. 5f. The *R* and *D** are calculated as the following equations:

$$R = \frac{(I_{photo} - I_d)/S}{P} \tag{2}$$

and

$$D^* = \frac{R}{\sqrt{2eI_d/S}} \tag{3}$$

where I_{photo} is the photocurrent, I_d is the dark current, *S* is the active area of the PD, and *P* is the light power density illuminated onto the device. Here, *S* is 7.85 × 10^{-7} m^2 (Fig. S23). As shown in Fig. 5f, the P4 film-based PD presents an average responsivity of 1 A W^{-1}, corresponding to detectivities of 1.5 × 10^{14} Jones.

Since the P4 film-based PDs demonstrate the highest performance, the photoresponse behaviors of the P4 film-based PD to 360 nm laser illumination are systematically investigated and summarized in Fig. S24

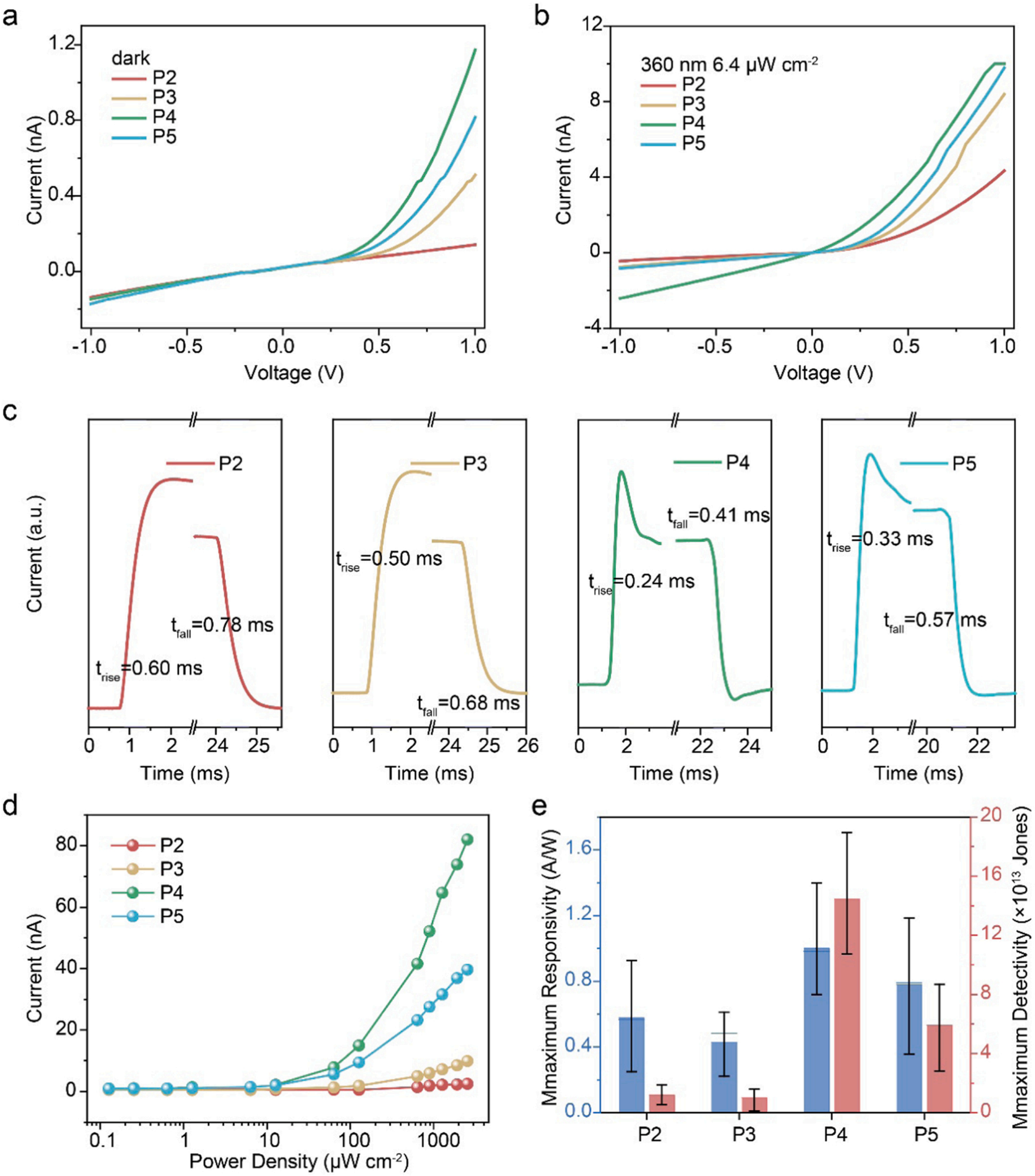

Fig. 5. *I-V* curves of P2-P5 films-based PDs under (a) dark condition and (b) light illumination with a power density of 6.4 μW cm^{-2}. (c) On-off photoresponses of P2-P5 films-based PDs measured under a modulation frequency of 2 Hz. (d) $I_{\mathrm{pyro+photo}}$-I_{pyro}, of P2-P5 films-based PDs as a function of the power density. (e) Statistics of responsivities and detectivities of P2-P5 films-based PDs.

by changing the power densities from 0 to 2547 μW cm^{-2}. When power density is less than 1.27 μW cm^{-2}, the four four-stage photoresponse behavior is apparent (inset in Fig. S24a). Further increasing the power density will result in the more unobvious negative pyroelectric current and slower decay speed of the positive pyroelectric current. The corresponding *R* is summarized in Fig. S24c, from which one can see that the *R* gradually decreases with the increase of power density. For lower power densities (less than 1 μW cm^{-2}), the photoresponsivity is significantly enhanced *via* the ferro-pyro-phototronic effect (Fig. S24d). The maximum *R* value is 1 A W^{-1} at the power density of 0.12 μW cm^{-2}, with the enhancement of 20 times by the ferro-pyro-phototronic effect. The corresponding performances for P2, P3, and P5 films-based PDs are shown in Figs. S25–S27, respectively. The photodetection performances of the previously reported self-powered UV PDs, self-powered perovskite-based PDs, and the present 2D-ferroelectric film-based PD are listed in Table 2. It is obvious that our UV PDs demonstrate the highest detectivity, short response/recovery time, and high photoresponsivity.

To further verify the enhancement and modulation function of ferro-pyro-phototronic effect in our PDs, we performed polarization tuning and switching test by varying the polarization voltage. The performances of the PDs are highly on the electric field of the spontaneous polarization. From Fig. S28, one can see that the when the polarization voltage is less than 0.4 V, the output currents gradually increase with the increase of the polarization voltage. The output currents reach saturation at a polarization voltage of 0.5 V. Further increasing the polarization voltage results in tiny changes of the output currents. Furthermore, the polarization direction switching of the ferroelectric films allow the modulation of output current directions. As shown in Fig. S29a, after

Table 2

Performance comparisons of reported self-powered UV photodetectors and perovskite photodetectors.

Active Materials	Wavelength (nm)	Responsivity (A W^{-1})	Detectivity (Jones)	Rise time (s)	Decay time (s)	Ref.
CdS/Si	325	5.9×10^{-3}	1.0×10^{12}	$\sim 2.5 \times 10^{-4}$	$\sim 2.7 \times 10^{-4}$	[41]
InSe/Au	365	0.369	2.56×10^{11}	0.068	0.075	[42]
GaN/Sn:Ga_2O_3	254	3.05	1.69×10^{13}	0.018	—	[43]
Multilayer γ-InSe	400	0.824	8.7×10^{11}	2.03×10^{-5}	1.08×10^{-5}	[44]
$BaTiO_3$ film	405	7.5×10^{-6}	$\sim 9 \times 10^{9}$	0.88	1.06	[14]
bis(dithiolene) iron(II) nanosheet	365	6.57×10^{-3}	3.13×10^{11}	~0.03	~0.03	[45]
ZnO NWs/SnS	365	1.55×10^{-4}	—	49.1	51.8	[46]
$(BPA)_2PbBr_4$	377	$\sim 10^{-4}$	$\sim 10^{7}$	2.7×10^{-5}	3×10^{-5}	[15]
NiO/PLZT heterojunction	350	6.3×10^{-4}	1.29×10^{10}	0.34	0.36	[47]
ZnO/PLZT heterojunction	360	3.96×10^{-3}	6.6×10^{10}	0.04	0.05	[48]
$(PMA)_2PbCl_4$	320	9	1.01×10^{11}	1.62×10^{-4}	2.26×10^{-4}	[49]
$(PEA)_2MA_3Pb_4I_{13}$	570	0.44	3.38×10^{12}	2.08×10^{-5}	2.06×10^{-5}	[26]
$CsPbBr_3$ QDs	530	10.1	9.35×10^{13}	2.3	—	[50]
Si/SnO_x/ZnO heterojunction	405	3.67×10^{-2}	1.5×10^{11}	3×10^{-6}	2×10^{-6}	[51]
$(BA)_2MA_3Pb_4Br_{13}$	360	1	1.54×10^{14}	2.6×10^{-4}	4.2×10^{-4}	This work

poled with opposite polarization voltage of – 0.5 V, opposite pyroelectric currents are observed when light is turned on. Furthermore, the signals of the open-circuit voltage (V_{oc}) are opposite with different polarization orientations (Fig. S29b). The above two results indicate that the photoresponse behaviors of the PDs are closely related to the ferroelectric polarization. Photogenerated electrons and holes will be driven by the spontaneous polarization induced built-in electric field. By changing the direction of the spontaneous polarization, the direction of the built-in field is reversed, leading to the photocurrents in opposite directions. For pyroelectric current, when the direction of the spontaneous polarization is reversed, the bound charges at the interface will be changed, leading to the opposite direction of free charges transport in the external circuit. Besides, we conducted another two experiments: 1, temperature-dependence of ferro-pyro-phototronic effect in P4 film-based PDs; 2, Comparison of the $(BA)_2(MA)_3Pb_4Br_{13}$ P4 film-based PDs with another two 2D perovskite films without ferroelectricity ($(iBA)_2(MA)_3Pb_4Br_{13}$ and $(tBA)_2(MA)_3Pb_4Br_{13}$, iBA is isobutylamine and tBA is tert-butylamine). Except for the structure of butyl, all the procedures for preparation of the perovskite films and devices are identical. From Fig. S30, one can see that once the testing temperature is above the Curie temperature of the P4 film (between 357 K and 372 K), the current peaks no longer appear. When the testing temperature returns to the room temperature, the current peaks continue to appear once the laser is turned on/off. From Fig. S31, one can see that no peak currents were observed for $(iBA)_2(MA)_3Pb_4Br_{13}$ and $(tBA)_2(MA)_3Pb_4Br_{13}$ perovskite films based PDs. Besides, the output currents of $(BA)_2(MA)_3Pb_4Br_{13}$ films are much larger than those films without ferroelectricity. Therefore, the ferro-pyro-phototronic effect-based PDs is strongly related to ferroelectric polarization.

In addition, we also evaluate the impact of switching frequency and bias voltage on photosensing performance. From Fig. S32, one can see that with the increase of the light switching frequency (0-30 Hz), the pyroelectric current gradually decreases while the photocurrent remains unchanged. Further increasing the frequency to 400 Hz will lead to the vanishing of pyroelectric current. Besides, the response time and recovery time decrease with the increase of frequency. The *I-t* curves under reverse bias voltages ranging from 0 to 1.6 V and forward bias voltages ranging from 0 to 1.6 V towards 360 nm laser illumination are shown in Fig. S33. With the increase of reverse bias, both the photocurrent and pyroelectric current are gradually decreased. The pyroelectric current finally vanishes when the bias exceeds – 1.6 V. This reduced output current can be inferred as that the reverse bias induced electric field is opposite to the heterojunction built-in electric field. With the increase of forward bias from 0.2 to 1.4 V, the photocurrent gradually increases while the four-stage photo-response dynamic behavior becomes more obvious. However, current mutation occurred at 1.6 V, where the pyroelectric response vanishes and the dark current undergoes a sharp increase, indicating that the working bias for our PDs should be less than 1.6 V. The weakened pyroelectric currents can be attributed to joule heat caused by the applied bias voltage [41].

Moreover, our PDs exhibited excellent humidity stability and thermal stability. As shown in Fig. 6, P4 film-based PDs with 4-FPEAI modification maintained 67.5% of their initial responses after being stored in ambient air (80 ± 5% RH) at RT for 32 days (Fig. 6a), and 58% of their initial responses after continuous heating at 80 °C in an N_2-filled glove box for 32 days (Fig. 6b). In contrast, the P4 film-based PDs without 4-FPEAI modification undergo degradation of 35% and 42% after 6 days under humidity and heating conditions, respectively (Fig. S34). In the future work, introducing the two-dimensional Dion-Jacobson perovskite to partially replace RP perovskite or preparing the methylamine-free perovskite could further enhance the stability of the devices. Furthermore, the PDs also demonstrated good reproducibility. We measured over 15 PDs' on-off photoresponses to evaluate the PDs' performances. Fig. S35 depicts averaged lowest detectable power density and maximum responsivity of the PDs, with relatively small distributions, showing good consistency.

4. Conclusion

In conclusion, the ferroelectric perovskite films with high crystallinity, narrow phase distribution, and preferred perpendicular orientation were obtained by ionic solvent assisted hot-spin-coating method and solvent engineering. It is found that the crystallinity, orientation, and phase distribution of the 2D perovskites can be effectively tailored by simply adjusting the solvent composition of the precursors. Then, self-powered 2D perovskite/PC61BM PDs were fabricated using the optimization condition. With the improved crystal quality, P4 film-based PD exhibits a high average maximum responsivity of over 1 A W^{-1}, and the maximum detectivity can reach 1.54×10^{14} Jones under 360 nm laser illumination, respectively. The device also displays a fast response/recovery time of 260/420 μs. Furthermore, owing to the ferro-pyro-phototronic effect, the corresponding photoconductive, specific detectivity, and responsivity of the photodetector can be boosted by over 160% at an illumination intensity of 127.6 μW cm^{-2} compared to that only using the photovoltaic effect. Moreover, the PDs modified with 4-FPEAI show high humidity and thermal stability. The ferro-pyro-photoelectric effect boosted self-powered PD based on 2D ferroelectric film provides a new idea and optimization method for realizing highly sensitive and self-powered photodetection, providing potential for future applications such as wearable electronics, broad spectral detection, fast optoelectronic detection and imaging.

CRediT authorship contribution statement

Linjuan Guo, **Yaqian Qi** and **Zheng Yang** contributed equally to this work. **Zheng Yang** conceived and supervised the project. **Linjuan**

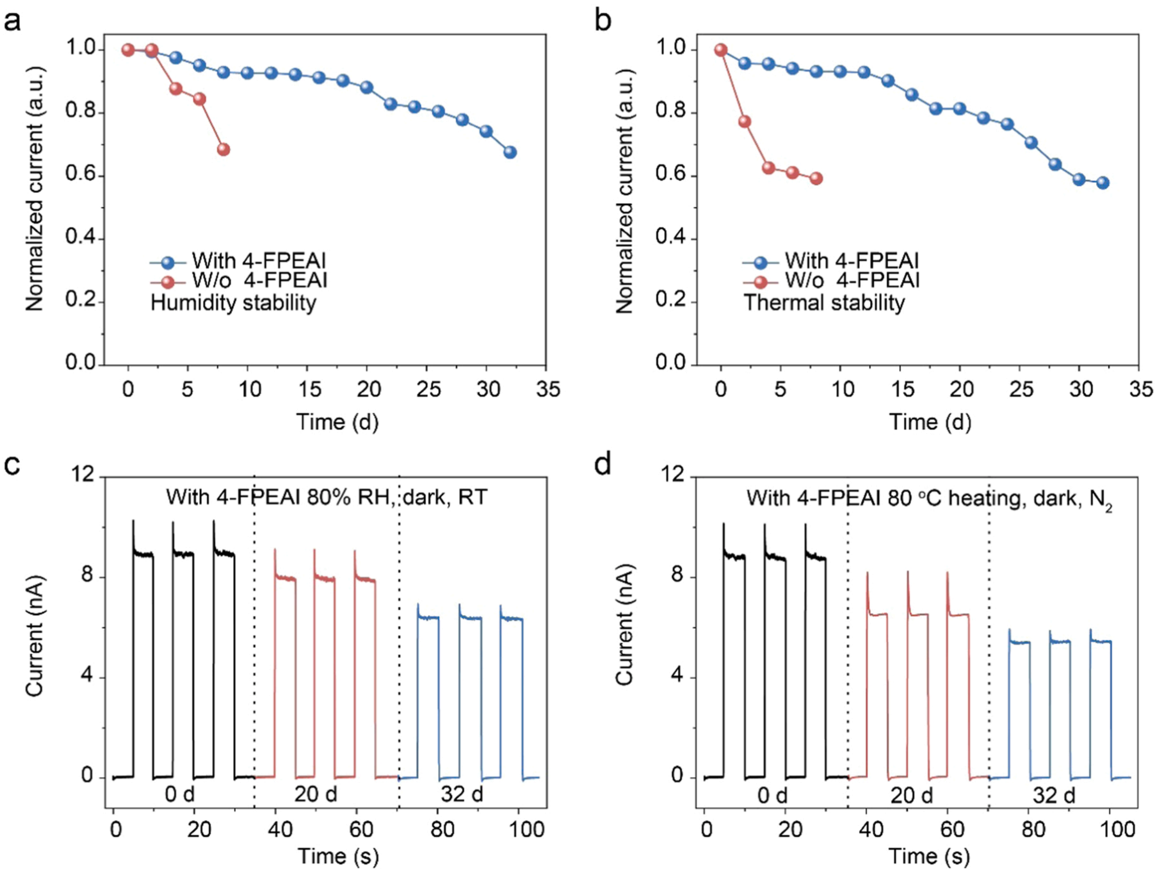

Fig. 6. Normalized output currents of PDs with and without 4-FPEAI modification (a) exposed to ambient atmosphere (80 ± 5% RH and RT) in dark condition and (b) heated at 80 °C in an N_2-filled glove box without encapsulation. (c, d) The corresponding *I-t* characteristics of the PDs with 4-FPEAI modification to the 360 nm laser illumination (127.3 μW cm^{-2}) after 0 and 32 days.

Guo and **Yaqian Qi** prepared the perovskites, fabricated the devices, and measured the optoelectronic properties. **Lei Zhao** and **Wei Zhang** contributed to the ferroelectric and permittivity measurement. **Xinzhan Wang** contributed to the PL measurement. **Haixu Liu** contributed to the UPS and XPS measurements. **Linjuan Guo** wrote the manuscript. **Zheng Yang** modified it. **Guoying Yan**, **Shufang Wang** and **Caofeng Pan** provided funding support and critical suggestions for this work. All the authors reviewed the manuscript.

Declaration of Competing Interest

The authors declare that they have no known competing financial interests or personal relationships that could have appeared to influence the work reported in this paper.

Data Availability

No data was used for the research described in the article.

Acknowledgments

This work was supported by the National Natural Science Foundation of China (Grant Nos. 62005072, 62104057, 51972094, 52125205, U20A20166, 61805015 and 61804011), the Natural Science Foundation of Hebei Province (Grant Nos. E2020201025, E2021201016, and B2021201034), Hebei Education Department (Grant No. BJK2022050), the Advanced Talents Incubation Program of the Hebei University (Grant Nos. 521000981287, 521000981351, and 521000981248), the Science and Technology Plan Project of Hebei Province (Grant No. 226Z1002G).

Appendix A. Supplementary material

Supplementary data associated with this article can be found in the online version at doi:10.1016/j.nanoen.2022.107714.

References

[1] J. Jeong, M. Kim, J. Seo, H. Lu, P. Ahlawat, A. Mishra, Y. Yang, M.A. Hope, F. T. Eickemeyer, M. Kim, Y.J. Yoon, I.W. Choi, B.P. Darwich, S.J. Choi, Y. Jo, J. H. Lee, B. Walker, S.M. Zakeeruddin, L. Emsley, U. Rothlisberger, A. Hagfeldt, D. S. Kim, M. Gratzel, J.Y. Kim, Pseudo-halide anion engineering for alpha-$FAPbI_3$ perovskite solar cells, Nature 592 (2021) 381–385.

[2] Y. Lei, Y. Chen, R. Zhang, Y. Li, Q. Yan, S. Lee, Y. Yu, H. Tsai, W. Choi, K. Wang, Y. Luo, Y. Gu, X. Zheng, C. Wang, C. Wang, H. Hu, Y. Li, B. Qi, M. Lin, Z. Zhang, S. A. Dayeh, M. Pharr, D.P. Fenning, Y.H. Lo, J. Luo, K. Yang, J. Yoo, W. Nie, S. Xu, A fabrication process for flexible single-crystal perovskite devices, Nature 583 (2020) 790–795.

[3] K. Lin, J. Xing, L.N. Quan, F.P.G. de Arquer, X. Gong, J. Lu, L. Xie, W. Zhao, D. Zhang, C. Yan, W. Li, X. Liu, Y. Lu, J. Kirman, E.H. Sargent, Q. Xiong, Z. Wei, Perovskite light-emitting diodes with external quantum efficiency exceeding 20 per cent, Nature 562 (2018) 245–248.

[4] C. Qin, A.S.D. Sandanayaka, C. Zhao, T. Matsushima, D. Zhang, T. Fujihara, C. Adachi, Stable room-temperature continuous-wave lasing in quasi-2D perovskite films, Nature 585 (2020) 53–57.

[5] E. Shi, B. Yuan, S.B. Shiring, Y. Gao, Akriti, Y. Guo, C. Su, M. Lai, P. Yang, J. Kong, B.M. Savoie, Y. Yu, L. Dou, Two-dimensional halide perovskite lateral epitaxial heterostructures, Nature 580 (2020) 614–620.

[6] X. Gao, X. Zhang, W. Yin, H. Wang, Y. Hu, Q. Zhang, Z. Shi, V.L. Colvin, W.W. Yu, Y. Zhang, Ruddlesden-Popper perovskites: synthesis and optical properties for optoelectronic applications, Adv. Sci. 6 (2019) 1900941.

[7] X. Li, J.M. Hoffman, M.G. Kanatzidis, The 2D halide perovskite rulebook: how the spacer influences everything from the structure to optoelectronic device efficiency, Chem. Rev. 121 (2021) 2230–2291.

[8] H. Xu, S. Han, Z. Sun, J. Luo, Recent advances of two-dimensional organic-inorganic hybrid perovskite ferroelectric materials, Acta Chim. Sin. 79 (2021) 23–35.

[9] W.Q. Liao, Y. Zhang, C.L. Hu, J.G. Mao, H.Y. Ye, P.F. Li, S.D. Huang, R.G. Xiong, A lead-halide perovskite molecular ferroelectric semiconductor, Nat. Commun. 6 (2015) 7338.

[10] Z. Xu, W. Weng, Y. Li, X. Liu, T. Yang, M. Li, X. Huang, J. Luo, Z. Sun, 3D-to-2D dimensional reduction for exploiting a multilayered perovskite ferroelectric toward polarized-light detection in the solar-blind ultraviolet region, Angew. Chem. Int. Ed. 59 (2020) 21693–21697.

[11] Z. Wu, C. Ji, L. Li, J. Kong, Z. Sun, S. Zhao, S. Wang, M. Hong, J. Luo, Alloying n-butylamine into $CsPbBr_3$ to give a two-dimensional bilayered perovskite ferroelectric material, Angew. Chem. Int. Ed. 57 (2018) 8140–8143.

[12] F. Cao, W. Tian, M. Wang, H. Cao, L. Li, Semitransparent, flexible, and self-powered photodetectors based on ferroelectricity-assisted perovskite nanowire arrays, Adv. Funct. Mater. 29 (2019) 1901280.

[13] Y. Zhang, J. Chen, L. Zhu, Z.L. Wang, Self-powered high-responsivity photodetectors enhanced by the pyro-phototronic effect based on a $BaTiO_3$/GaN heterojunction, Nano Lett. 21 (2021) 8808–8816.

[14] K. Zhao, B. Ouyang, C.R. Bowen, Y. Yang, Enhanced photocurrent via ferro-pyro-phototronic effect in ferroelectric $BaTiO_3$ materials for a self-powered flexible photodetector system, Nano Energy 77 (2020), 105152.

[15] C. Ji, D. Dey, Y. Peng, X. Liu, L. Li, J. Luo, Ferroelectricity-driven self-powered ultraviolet photodetection with strong polarization sensitivity in a two-dimensional halide hybrid perovskite, Angew. Chem. Int. Ed. 59 (2020) 18933–18937.

[16] L. Li, X. Liu, Y. Li, Z. Xu, Z. Wu, S. Han, K. Tao, M. Hong, J. Luo, Z. Sun, Two-dimensional hybrid perovskite-type ferroelectric for highly polarization-sensitive shortwave photodetection, J. Am. Chem. Soc. 141 (2019) 2623–2629.

[17] A.Z. Chen, M. Shiu, X. Deng, M. Mahmoud, D. Zhang, B.J. Foley, S.-H. Lee, G. Giri, J.J. Choi, Understanding the formation of vertical orientation in two-dimensional metal halide perovskite thin films, Chem. Mater. 31 (2019) 1336–1343.

[18] A.Z. Chen, M. Shiu, J.H. Ma, M.R. Alpert, D. Zhang, B.J. Foley, D.M. Smilgies, S. H. Lee, J.J. Choi, Origin of vertical orientation in two-dimensional metal halide perovskites and its effect on photovoltaic performance, Nat. Commun. 9 (2018) 1336.

[19] K. Wang, C. Wu, D. Yang, Y. Jiang, S. Priya, Quasi-two-dimensional halide perovskite single crystal photodetector, ACS Nano 12 (2018) 4919–4929.

[20] H. Li, T. Luo, S. Zhang, Z. Sun, X. He, W. Zhang, H. Chang, Two-dimensional metal-halide perovskite-based optoelectronics: synthesis, structure, properties and applications, Energy Environ. Mater. 4 (2020) 46–64.

[21] X. Zhang, T. Yang, X. Ren, L. Zhang, K. Zhao, S. Liu, Film formation control for high performance Dion-Jacobson 2D perovskite solar cells, Adv. Energy Mater. 11 (2021) 2002733.

[22] C. Liang, H. Gu, Y. Xia, Z. Wang, X. Liu, J. Xia, S. Zuo, Y. Hu, X. Gao, W. Hui, L. Chao, T. Niu, M. Fang, H. Lu, H. Dong, H. Yu, S. Chen, X. Ran, L. Song, B. Li, J. Zhang, Y. Peng, G. Shao, J. Wang, Y. Chen, G. Xing, W. Huang, Two-dimensional Ruddlesden-Popper layered perovskite solar cells based on phase-pure thin films, Nat. Energy 6 (2020) 38–45.

[23] W. Hui, L. Chao, H. Lu, F. Xia, Q. Wei, Z. Su, T. Niu, L. Tao, B. Du, D. Li, Y. Wang, H. Dong, S. Zuo, B. Li, W. Shi, X. Ran, P. Li, H. Zhang, Z. Wu, C. Ran, L. Song, G. Xing, X. Gao, J. Zhang, Y. Xia, Y. Chen, W. Huang, Stabilizing black-phase formamidinium perovskite formation at room temperature and high humidity, Science 371 (2021) 1359–1364.

[24] G. Li, Z. Su, M. Li, F. Yang, M.H. Aldamasy, J. Pascual, F. Yang, H. Liu, W. Zuo, D. Di Girolamo, Z. Iqbal, G. Nasti, A. Dallmann, X. Gao, Z. Wang, M. Saliba, A. Abate, Ionic liquid stabilizing high-efficiency tin halide perovskite solar cells, Adv. Energy Mater. 11 (2021) 2101539.

[25] C.C. Boyd, R. Cheacharoen, T. Leijtens, M.D. McGehee, Understanding degradation mechanisms and improving stability of perovskite photovoltaics, Chem. Rev. 119 (2019) 3418–3451.

[26] L. Min, W. Tian, F. Cao, J. Guo, L. Li, 2D Ruddlesden-Popper perovskite with ordered phase distribution for high-performance self-powered photodetectors, Adv. Mater. 33 (2021) 2101714.

[27] H. Zhang, K. Li, M. Sun, F. Wang, H. Wang, A.K.Y. Jen, Design of superhydrophobic surfaces for stable perovskite solar cells with reducing lead leakage, Adv. Energy Mater. 11 (2021) 2102281.

[28] X. Min, F. Jiang, F. Qin, Z. Li, J. Tong, S. Xiong, W. Meng, Y. Zhou, Polyethylenimine aqueous solution: a low-cost and environmentally friendly formulation to produce low-work-function electrodes for efficient easy-to-fabricate organic solar cells, ACS Appl. Mater. Interfaces 6 (2014) 22628–22633.

[29] Z. Dai, S.K. Yadavalli, M. Chen, A. Abbaspourtamijani, Y. Qi, N.P. Padture, Interfacial toughening with self-assembled monolayers enhances perovskite solar cell reliability, Science 372 (2021) 618–623.

[30] X.-J. She, C. Chen, G. Divitini, B. Zhao, Y. Li, J. Wang, J.F. Orri, L. Cui, W. Xu, J. Peng, S. Wang, A. Sadhanala, H. Sirringhaus, A solvent-based surface cleaning and passivation technique for suppressing ionic defects in high-mobility perovskite field-effect transistors, Nat. Electron. 3 (2020) 694–703.

[31] L. Li, Z. Sun, P. Wang, W. Hu, S. Wang, C. Ji, M. Hong, J. Luo, Tailored engineering of an unusual $(C_4H_9NH_3)_2(CH_3NH_3)_2Pb_3Br_{10}$ two-dimensional multilayered perovskite ferroelectric for a high-performance photodetector, Angew. Chem. Int. Ed. 56 (2017) 12150–12154.

[32] C.M.M. Soe, W. Nie, C.C. Stoumpos, H. Tsai, J.-C. Blancon, F. Liu, J. Even, T. J. Marks, A.D. Mohite, M.G. Kanatzidis, Understanding film formation morphology and orientation in high member 2D Ruddlesden-Popper perovskites for high-efficiency solar cells, Adv. Energy Mater. 8 (2018) 1700979.

[33] J.C. Blancon, H. Tsai, W. Nie, C.C. Stoumpos, L. Pedesseau, C. Katan, M. Kepenekian, C.M.M. Soe, K. Appavoo, M.Y. Sfeir, S. Tretiak, P.M. Ajayan, M. G. Kanatzidis, J. Even, J.J. Crochet, A.D. Mohite, Perovskite physics extremely efficient internal exciton dissociation through edge states in layered 2D perovskites, Science 355 (2017) 1288–1291.

[34] Y. Qin, H. Zhong, J.J. Intemann, S. Leng, M. Cui, C. Qin, M. Xiong, F. Liu, A.K. Y. Jen, K. Yao, Coordination engineering of single-crystal precursor for phase control in ruddlesden-popper perovskite solar cells, Adv. Energy Mater. 10 (2020) 2101714.

[35] Y. Lin, Y. Fang, J. Zhao, Y. Shao, S.J. Stuard, M.M. Nahid, H. Ade, Q. Wang, J. E. Shield, N. Zhou, A.M. Moran, J. Huang, Unveiling the operation mechanism of layered perovskite solar cells, Nat. Commun. 10 (2019) 1008.

[36] S. Wu, R. Chen, S. Zhang, B.H. Babu, Y. Yue, H. Zhu, Z. Yang, C. Chen, W. Chen, Y. Huang, S. Fang, T. Liu, L. Han, W. Chen, A chemically inert bismuth interlayer enhances long-term stability of inverted perovskite solar cells, Nat. Commun. 10 (2019) 1161.

[37] E.H. Jung, N.J. Jeon, E.Y. Park, C.S. Moon, T.J. Shin, T.Y. Yang, J.H. Noh, J. Seo, Efficient, stable and scalable perovskite solar cells using poly(3-hexylthiophene), Nature 567 (2019) 511–515.

[38] W. Pan, M. Tan, Y. He, H. Wei, B. Yang, Organic amine-bridged quasi-2D perovskite/PbS colloidal quantum dots composites for high-gain near-infrared photodetectors, Nano Lett. 22 (2022) 2277–2284.

[39] Y. Zhang, M. Hu, Z. Wang, Enhanced performances of p-si/n-ZnO self-powered photodetector by interface state modification and pyro-phototronic effect, Nano Energy 71 (2020), 104630.

[40] B. Wang, Y. Zhu, J. Dong, J. Jiang, Q. Wang, S. Li, X. Wang, Self-powered, superior high gain silicon-based near-infrared photosensing for low-power light communication, Nano Energy 70 (2020), 104544.

[41] Y. Dai, X. Wang, W. Peng, C. Xu, C. Wu, K. Dong, R. Liu, Z.L. Wang, Self-powered Si/CdS flexible photodetector with broadband response from 325 to 1550 nm based on pyro-phototronic effect: an approach for photosensing below bandgap energy, Adv. Mater. 30 (2018) 1705893.

[42] M. Dai, H. Chen, R. Feng, W. Feng, Y. Hu, H. Yang, G. Liu, X. Chen, J. Zhang, C.-Y. Xu, A dual-band multilayer InSe self-powered photodetector with high performance induced by surface plasmon resonance and asymmetric Schottky junction, ACS Nano 12 (2018) 8739–8747.

[43] D. Guo, Y. Su, H. Shi, P. Li, N. Zhao, J. Ye, S. Wang, A. Liu, Z. Chen, C. Li, Self-powered ultraviolet photodetector with superhigh photoresponsivity (3.05 A/W) based on the GaN/Sn: Ga_2O_3 pn junction, ACS Nano 12 (2018) 12827–12835.

[44] M. Dai, H. Chen, F. Wang, Y. Hu, S. Wei, J. Zhang, Z. Wang, T. Zhai, P. Hu, Robust piezo-phototronic effect in multilayer γ-InSe for high-performance self-powered flexible photodetectors, ACS Nano 13 (2019) 7291–7299.

[45] Y.C. Wang, C.H. Chiang, C.M. Chang, H. Maeda, N. Fukui, I.T. Wang, C.Y. Wen, K. C. Lu, S.K. Huang, W.B. Jian, Two-dimensional bis (dithiolene) iron (II) self-powered UV photodetectors with ultrahigh air stability, Adv. Sci. 8 (2021) 2100564.

[46] B. Ouyang, K. Zhang, Y. Yang, Photocurrent polarity controlled by light wavelength in self-powered ZnO nanowires/SnS photodetector system, iScience 1 (2018) 16–23.

[47] J. Chen, D. You, Y. Zhang, T. Zhang, C. Yao, Q. Zhang, M. Li, Y. Lu, Y. He, Highly sensitive and tunable self-powered UV photodetectors driven jointly by pn junction and ferroelectric polarization, ACS Appl. Mater. Interfaces 12 (2020) 53957–53965.

[48] J. Chen, Z. Wang, H. He, J. Mao, Y. Zhang, Q. Zhang, M. Li, Y. Lu, Y. He, High-performance self-powered ultraviolet photodetector based on coupled ferroelectric depolarization field and heterojunction built-in potential, Adv. Electron. Mater. 7 (2021) 2100717.

[49] L. Guo, X. Liu, L. Gao, X. Wang, L. Zhao, W. Zhang, S. Wang, C. Pan, Z. Yang, Ferro-pyro-phototronic effect in monocrystalline 2D ferroelectric perovskite for high-sensitive, self-powered, and stable ultraviolet photodetector, ACS Nano 46 (2022) 1280–1290.

[50] K. Shen, H. Xu, X. Li, J. Guo, S. Sathasivam, M. Wang, A. Ren, K.L. Choy, I. P. Parkin, Z. Guo, Flexible and self-powered photodetector arrays based on all-inorganic $CsPbBr_3$ quantum dots, Adv. Mater. 32 (2020) 2000004.

[51] J.P.B. Silva, E.M.F. Vieira, K. Gwozdz, A. Kaim, L.M. Goncalves, J.L. MacManus-Driscoll, R.L.Z. Hoye, M. Pereira, High-performance self-powered photodetectors achieved through the pyro-phototronic effect in Si/SnO_x/ZnO heterojunctions, Nano Energy 89 (2021), 106347.

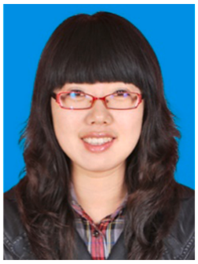

Dr. Linjuan Guo obtained her Ph.D. in Xinjiang Technical Institute of Physics & Chemistry, CAS in 2017. Then she joined the College of Physics Science and Technology at Hebei University in 2019. Her research interest mainly focuses on the design, preparation and optoelectronics applications of 2D perovskites.

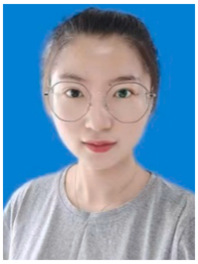

Yaqian Qi is currently a graduate student at the College of Physical Science and Technology, Hebei University. Her current research focuses on 2D Ruddlesden-Popper perovskite ferroelectric films and their photoelectric applications.

Dr. Zheng Yang received his Ph.D. degree in Nanoscience and Nanotechnology from the Beijing Institute of Nanoenergy and Nanosystems (CAS) in 2019. Now he is an associate professor in the College of Physics Science and Technology at Hebei University. His research is mainly focused on the controllable growth and optoelectronics applications of lead halide perovskites.

Dr. Lei Zhao is now an associate professor at Hebei University, China. He received his Ph.D. degree in Materials Science and Engineering from University of Science and Technology Beijing in 2015. His main research interests focus on the dielectric and ferroelectric materials.

Dr. Wei Zhang received his Ph.D degree from Soochow University in 2016. He then joined the College of Physics Science and Technology at Hebei University. His research interests include magnetoelectric functional materials, 2D materials, as well as their electronic and optoelectronic devices.

Dr. Xinzhan Wang received his Ph.D. degree in Optical Engineering from Hebei University in 2014. Then he joined the College of Physics Science and Technology at Hebei University. His research is mainly focused on the optoelectronic applications of lead halide perovskites.

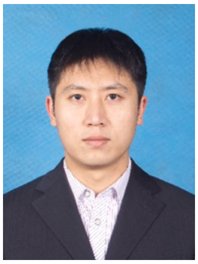

Dr. Haixu Liu received his Ph.D. degree in Condensed matter physics from the Nankai University (NKU) in 2011. Then he joined the College of Physics Science and Technology at Hebei University. His research interest is mainly focused on the preparation of novel optoelectronics thin films and the fabrication of long-term stable perovskites solar cells (PSCs).

Dr. Guoying Yan received her Ph. D. Degree in Electronic Science and Technology from Hebei University of Technology in 2016. Now she is an associate professor in Collage of Physical Science and Technology, Hebei University. Her research interest is focused on the preparation and photo-thermal-electric conversion properties of the functional thin films.

Dr. Shufang Wang received her Ph.D. degree in Optics from the Institute of Physics, Chinese Academy of Sciences in 2004. She then joined in the group of Professor D. Rémiens at IEMN-CNRS, France as a postdoctral fellow and after that joined in the group of Professor Xiaoxing Xi at the Penn. State University as a postdoctral fellow. She is currently a full professor and a group leader at Hebei University of China. Her researches focus on the fields of photoelectric/thermoelectric materials and devices.

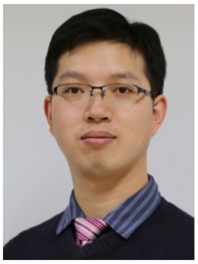

Dr. Caofeng Pan received his B.S. degree (2005) and his Ph.D. (2010) in Materials Science and Engineering from Tsinghua University, China. He then joined the Georgia Institute of Technology as a postdoctoral fellow. He is currently a professor and a group leader at the Beijing Institute of Nanoenergy and Nanosystems, Chinese Academy of Sciences since 2013. His main research interests focus on the fields of piezotronics/piezo-phototronics for fabricating new electronic and optoelectronic devices, nano-power sources (such as nanofuel cell, nano biofuel cell and, nanogenerator), hybrid nanogenerators, and self-powered nanosystems. Details can be found at http://piezotronics.binncas.cn/index%20en.php.